Journal of Power Sources 196 (2011) 4515–4523

Contents lists available at ScienceDirect

Journal of Power Sources

journal homepage: www.elsevier.com/locate/jpowsour

# Performance and stability of Pd–Pt–Ni nanoalloy electrocatalysts in proton exchange membrane fuel cells

Juan Zhao, Karalee Jarvis, Paulo Ferreira, Arumugam Manthiram*

*Electrochemical Energy Laboratory & Materials Science and Engineering Program, The University of Texas, Austin, TX 78712, United States*

ARTICLE INFO

*Article history:*
Received 14 November 2010
Received in revised form
30 December 2010
Accepted 7 January 2011
Available online 19 January 2011

*Keywords:*
Fuel cell
Electrocatalyst
Core–shell structure
Catalyst durability

ABSTRACT

Pd–Pt–Ni nanoalloy catalysts have been synthesized by a polyol reduction method and characterized for the oxygen reduction reaction (ORR) in proton exchange membrane fuel cells (PEMFCs). The performance of the membrane-electrode assembly (MEA) fabricated with the Pd–Pt–Ni catalysts is found to increase continuously in the entire current density range with the operation time in the PEMFC until it becomes comparable to that of commercial Pt. The Pt-based mass activity of Pd–Pt–Ni exceeds that of commercial Pt by a factor of 2, and its long-term durability is comparable to that of commercial Pt within the 200 h of operation. Compositional characterizations by energy dispersive spectroscopy (EDS) and X-ray photoelectron spectroscopy (XPS) suggest a dealloyed active catalyst phase consisting of Pd-rich core and Pt-rich shell, formed by dissolution of Pd and Ni under the testing conditions. The surface catalytic activity of nanoparticles can be modified by the strain effect caused by lattice mismatch between the surface and core components. Transmission electron microscopy (TEM) observation of the MEA cross-section reveals that the Pd ions move into the Nafion membrane and even to the anode side and redeposit on reduction by hydrogen crossover. The deposition of Pd-rich PdPt particles mainly forms a band at the center of the membrane and along the cathode/membrane interface. On the other hand, the Ni ions ion-exchange with the protons in the Nafion membrane.



## 1. Introduction

Proton exchange membrane fuel cells (PEMFCs) are attractive power sources due to their high efficiency and environmental friendliness compared to the conventional power sources [1–6]. However, the high cost of Pt electrocatalyst is one of the major barriers for the commercialization of PEMFCs. In this regard, there has been intensive effort to decrease Pt loading and improve catalytic activity, with a focus on both Pt-based catalysts [7–10] and non-platinum catalysts [11,12].

In the last several decades, Pt–M alloys (M is the transition metals) have been extensively investigated as cathode electrocatalysts in PEMFCs [13–25]. Pt-rich Pt–Co catalysts [11,26] have shown significant improvement in terms of Pt-mass-based performance. Their Pt-mass-based activities toward ORR have shown an improvement of up to 3 times compared to pure Pt. Recently, more attention has been focused on forming core–shell materials, either non-noble metal rich alloy catalysts with a Pt monolayer/skin on the surface or Pt-enriched nanpoparticle shell with a bimetallic core. These structures have been obtained by surface galvanic displacement reactions on glassy carbon [27–31] or in aqueous media [32–34], Pt overgrowth (encapsulation by Pt) [35–37], and surface metal depletion [38–40]. Previous work on galvanic displacement of under-potential deposited (UPD) Cu by Pt is limited mainly to basic catalytic research on glassy carbon electrodes [41]. Recently, Ball et al. [42] have carried out preliminary MEA tests that show great promise of $Pt_{ML}/Pd_3Co$ with a mass activity of up to 2 times compared to that of Pt. Another novel class of highly active electocatalysts have been developed by Strasser's group [39,40] by *in situ* voltammetric dealloying inside the cathode layer of MEAs, and a four to five fold improvement in Pt-mass activity in single PEMFCs has been reported.

Non-noble metal catalysts such as transition metal chalcogenides [43–45], transition metal oxides [46,47], transition metal macrocycles [48–50], and transition metal carbides or nitrides [51–54] have also been investigated as substitutes for Pt. However, their chemical instability in acidic environment and low intrinsic activities for the oxygen reduction reaction (ORR) due to the low density of active sites make these catalysts unattractive for practical application in PEMFCs. Recently, Pd-based alloy catalysts have been found to exhibit high activity for ORR with good tolerance to methanol [55–58]. However, the dissolution of both the transitional metal and Pd limits their application in fuel cells. One possible way to overcome the dissolution and improve the stability of these catalysts is to prepare nanoparticles with Pd–M at the core and Pt at the shell [33,36,37]. Although the base metal could dissolve and leach

* Corresponding author. Tel.: +1 512 471 1791; fax: +1 512 471 7681.
*E-mail address:* rmanth@mail.utexas.edu (A. Manthiram).

0378-7753/$ – see front matter © 2011 Elsevier B.V. All rights reserved.
doi:10.1016/j.jpowsour.2011.01.026

out completely over time, the dissolution of Pd may be alleviated [42].

We explored previously Pd–Ni nanoalloys for ORR [59] and found they are not stable enough in acid electrolytes. In this paper, we aim to improve both the performance and durability by alloying Pd–Ni with a small amount of Pt. Interestingly, the performance of Pd–Pt–Ni in single cell PEMFC increases continuously with operating time in the whole current density region and finally reaches a value similar to that of commercial Pt. The catalyst is also found to be as stable as commercial Pt within 200 h of operation. Accordingly, we present here the structural and compositional characterizations of the Pd–Pt–Ni electrocatalysts before and after the PEMFC operation and discuss the influence of the dissolution of both Pd and Ni on the ORR activity and the durability of Pd–Pt–Ni in PEMFC. Although there have been reports on the dissolution of Pd in acid [60,61] and formation of Pt skin upon dissolution of the transition metals [7,62–64], we show here, for the first time, that the dissolution of Pd and Ni during the operation of the membrane-electrode assemblies (MEA) in PEMFC results in the formation of a "Pd-rich core and Pt-rich shell" structure with enhanced catalytic activity.

## 2. Experimental methods

### 2.1. Catalyst synthesis

The Pd–Pt–Ni nanoparticle electrocatalysts were synthesized by a modified polyol reduction method as described elsewhere [59]. $(NH_4)_2PdCl_4$ (Alfa Aesar), $Ni(CH_3COO)_2{\cdot}6H_2O$ (Acros Organics), and $H_2PtCl_6$ (Strem Chemicals), together with Vulcan XC-72R carbon black (Cabot Corp.) as a supporting material and poly(vinylpyrrolidone) (PVP, MW = 40,000, MP Biomedicals, LLC) as a surfactant, were dissolved in ethylene glycol (Fisher Scientific) and kept under constant stirring until a homogeneous mixture was formed. NaOH (Fisher Scientific) was then added to adjust the pH value to 10, and the mixture was refluxed, filtered, washed, and dried overnight. The resulting black powder was subsequently heat-treated at 300 °C in a flowing 10% $H_2$–90% Ar atmosphere for 2 h and cooled to room temperature.

### 2.2. MEA fabrication

Catalyst inks were prepared by mixing required amounts of the carbon-supported catalyst, isopropyl alcohol, water, and 25 wt.% Nafion by ultrasonication for half an hour. The prepared catalyst ink was then directly sprayed onto the top of a commercial gas diffusion layer (BASF) (2.5 cm × 2.5 cm), followed by drying in air at 60 °C for 1 h. The metal loading was kept at 0.4 mg cm$^{-2}$ both for the anode and the cathode in the PEMFC. Thereafter, 40 mg of 5 wt.% Nafion solution was sprayed for better adhesion between the membrane and the catalyst-coated gas diffusion layer. For the anode layer, a commercial 20 wt.% Pt/C (Alpha Aesar) was used. The MEAs were fabricated by sandwiching a Nafion 112 membrane (DuPont) between the anode and cathode by hot-pressing at 130 °C and 1000 psi (6894.76 kPa) for 2 min.

### 2.3. Fuel cell testing

The prepared MEAs with an active area of 5 cm$^2$ were then assembled with 3-channel serpentine flow fields (Poco graphite blocks) and gold-coated current collectors and tested in a fuel cell station (Scribner In.), following the protocol shown in Fig. 1. In step 1, hydrogen and oxygen as reactant gases were supplied to the anode and cathode, respectively, without applying the load and the cell was stabilized at the open circuit potential for ~15 min; in step 2, the load was increased from 0 to 5 A (1000 mA cm$^{-2}$)

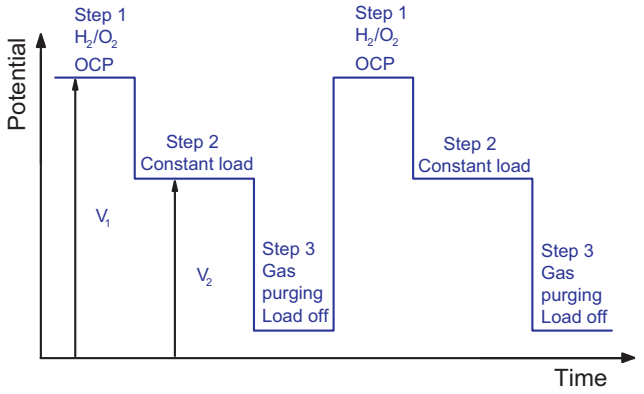


**Fig. 1.** The protocol applied for single cell fuel cell testing. Step 1: supplying reactant gases (hydrogen and air), step 2: operating the cell at the constant load of 5 A (1000 mA cm$^{-2}$), and step 3: purging nitrogen and removing the load.

at an increment of 0.5 A min$^{-1}$ for 10 min, and the cell was operated at a constant load of 5 A; in step 3, the load was removed, and the cell was shut down for overnight after 15 min of purging with nitrogen to remove the residual $H_2$ or $O_2$. The load cycles are employed in this study in an attempt to simulate the on/off procedures in real automotive application. Throughout the procedure, the relative humidity of the feed streams for the anode and cathode were set at 100% with a backpressure of, respectively, 14 psi (96.53 kPa) and 16 psi (110.32 kPa) and a constant gas flow rate of, respectively, 0.15 L min$^{-1}$ and 0.2 L min$^{-1}$; the cell temperature

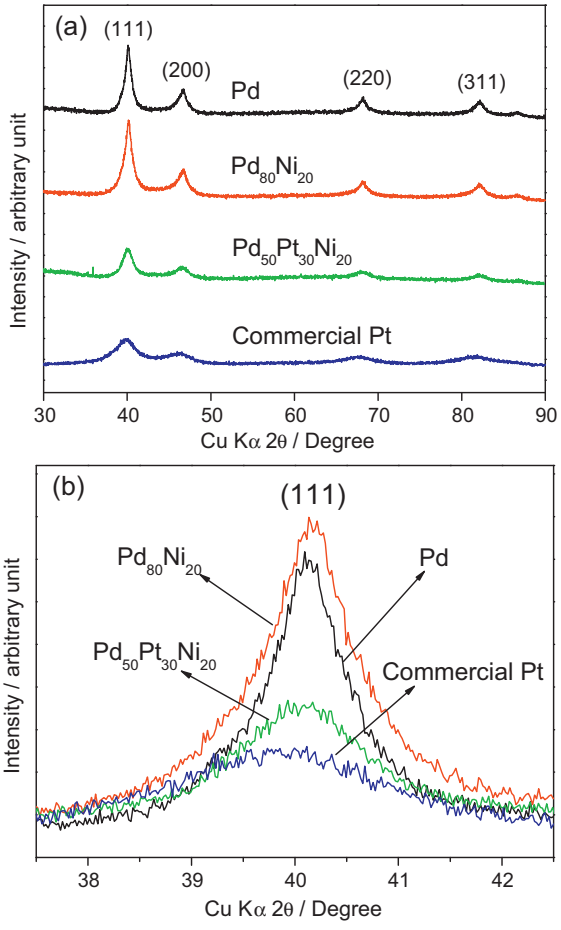


**Fig. 2.** (a) XRD patterns and (b) the enlarged (1 1 1) region of Pd, $Pd_{80}Ni_{20}$, and $Pd_{50}Pt_{30}Ni_{20}$ synthesized by the modified polyol method and commercial Pt.

**Table 1**
Atomic ratios, lattice parameters, and crystallite sizes of the samples synthesized by the modified polyol method and commercial Pt.

| Catalyst | Annealing temp. (°C) | Pd:Pt:Ni atomic ratio from SEM-EDS | Lattice parameter from XRD (nm) | Mean crystallite size from XRD (nm) |
|---|---|---|---|---|
| Pt | | | 0.3919 | 2.4 |
| Pd | 300 | | 0.3892 | 7.7 |
| $Pd_{80}Ni_{20}$ | 300 | 84:16 | 0.3888 | 6.2 |
| $Pd_{50}Pt_{30}Ni_{20}$ | 300 | 58:31:12 | 0.3896 | 5.1 |

was kept at 60 °C. The polarization curves were taken at the beginning and end of the test each day to monitor the performance change. Also, the cell voltage response with time at the constant load was recorded for long-term durability. IR correction was carried out by correcting the cell voltage with the measured ohmic resistance of the fuel cell by an in-built AC impedance analyzer operating at 1 kHz frequency.

### *2.4. Structural, morphological, and compositional characterization of catalyst powders and MEAs*

The phase identification of the catalyst powders was performed by X-ray diffraction (XRD) with Cu Kα radiation (λ = 0.154 nm) with a counting time of 12 s per 0.02°. The morphology and size distribution of the catalyst powders were studied with a JEOL 2010F transmission electron microscope (TEM) operating at 200 keV. The bulk compositional analysis was determined by energy dispersive spectroscopy (EDS) with a JEOL-JSM 5610 SEM having an Oxford Instruments EDS attachment. Surface compositions were assessed by X-ray photoelectron spectrometer (XPS) with Al Kα radiation. The experimental precisions associated with the EDS and XPS methods were estimated to be, respectively, about 3 and 2 atom%. The water collected from the cathode side after the durability test was analyzed by an inductively coupled plasma (ICP) analyzer to estimate the dissolution of metals from the catalyst particles. The cross-sections of MEAs were observed in a JEOL 2010F TEM/STEM equipped with an OXFORD energy dispersive spectrometer (EDS) to determine the elemental distri-

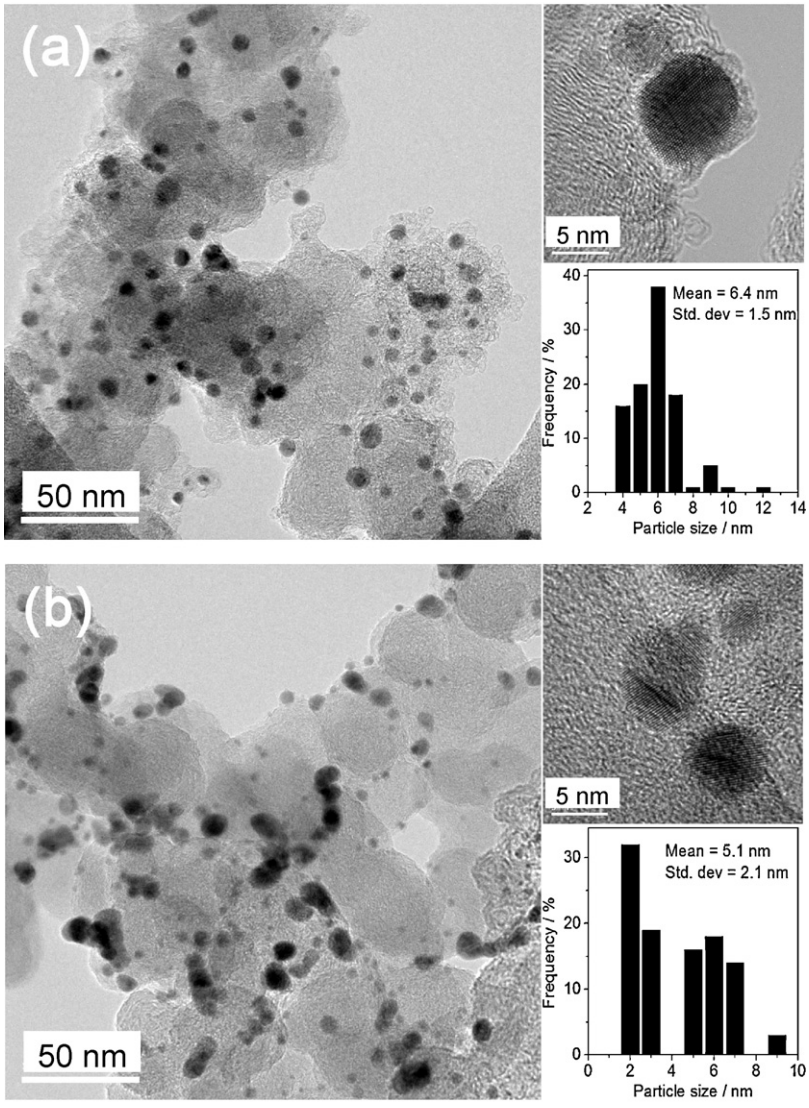


**Fig. 3.** TEM/HRTEM images and particle size distributions of (a) $Pd_{80}Ni_{20}$ and (b) $Pd_{50}Pt_{30}Ni_{20}$ synthesized by the modified polyol method.

bution across the MEAs before and after the fuel cell durability test.

## 3. Results and discussion

### 3.1. Physical characterization of the Pd–Pt–Ni electrocatalysts

Fig. 2 compares the XRD patterns of Pd, $Pd_{80}Ni_{20}$, and $Pd_{50}Pt_{30}Ni_{20}$ synthesized by the modified polyol method and commercial Pt. All samples exhibit reflections characteristic of a single fcc structure, suggesting a good mixing of all the constitutes and the formation of a ternary Pd–Pt–Ni alloy phase. From the enlarged profiles of the (1 1 1) reflection in Fig. 2(b), the reflections of $Pd_{80}Ni_{20}$ shift to higher angles compared to those in Pd, indicating the substitution of smaller Ni for Pd in the lattice. In addition, the diffraction peaks of $Pd_{50}Pt_{30}Ni_{20}$ shift to lower angles compared to those of $Pd_{80}Ni_{20}$, and even those of Pd, suggesting the incorporation of larger Pt atoms into the Pd–Ni lattice. The absence of peaks for either Pt, or Ni, or their oxides may be due to their poor crystallinity or low concentration. The lattice parameters and average crystallite sizes of these samples obtained from the XRD data using Scherrer equation are given in Table 1.

Fig. 3 shows the TEM images and particle size distributions of $Pd_{80}Ni_{20}$ and $Pd_{50}Pt_{30}Ni_{20}$ synthesized by the modified polyol method. The high resolution TEM images indicate a well-defined crystalline nature of the samples obtained. The ternary catalyst $Pd_{50}Pt_{30}Ni_{20}$ shows smaller particle size but with broader size distribution compared to the binary catalyst $Pd_{80}Ni_{20}$. Moreover, the TEM images reveal a higher agglomeration of the particles on the carbon support in the case of the ternary alloy, suggesting poor dispersion.

### 3.2. Electrochemical characterization of Pd–Pt–Ni electrocatalysts: MEA performance and long-term durability

Fig. 4(a) shows the polarization curves of $Pd_{50}Pt_{30}Ni_{20}$ recorded each day at the beginning and end of the fuel cell test until it became constant on the 8th day. As seen, the cell performance keeps increasing on the entire current range with time, and the increase is significant for the first four days and becomes smaller for the following days. The obvious increase from the 1st day to 2nd day is primarily due to the activation process. After the MEA assembly and the initial 4 h of operation, both the membrane and the electrode became humidified, and the contact between the flow-field plates and the diffusion media became better. Therefore, the electrolyte resistance, the contact resistance, and the resistance within the electrode became much smaller. Afterwards, the curves move upwards both within the day and between the two sequential days. The change within the day is much smaller compared to that between the two sequential days. Although the MEA structure may still keep optimizing in the following days, the extent of performance enhancement caused by the MEA structure optimization is small. Fig. 4(b) compares the constant polarization curves of $Pd_{50}Pt_{30}Ni_{20}$ and commercial Pt tested under the same condition and following the same procedure. The two curves overlap below 750 mA $cm^{-2}$, and $Pd_{50}Pt_{30}Ni_{20}$ even shows better performance in the higher current density region (also the ohmic resistance dominant region).

Fig. 5 and Table 2 show the kinetic activities after IR-correction for both $Pd_{50}Pt_{30}Ni_{20}$ and commercial Pt based on Pt mass alone (Fig. 5(a)) and noble metal mass (Fig. 5(b)). Here, the kinetic activities are compared at 0.84 V instead of at 0.9 V due to the low OCV and the change in Tafel slope at higher voltages. The Pt-based mass activity of commercial Pt is 0.392 A $mg_{Pt}^{-1}$ at 0.84 V, which is comparable to the values reported by other groups, considering possible

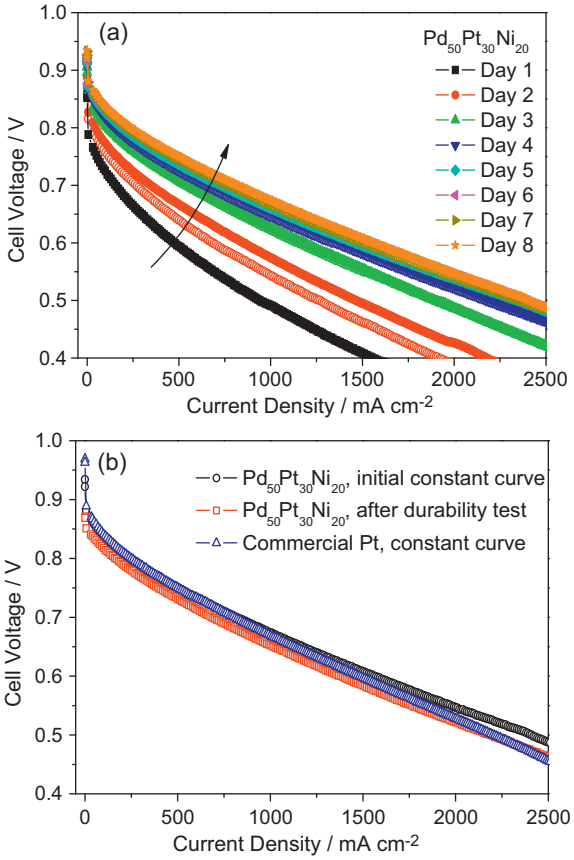


**Fig. 4.** (a) Performances of the $Pd_{50}Pt_{30}Ni_{20}$ catalyst, recorded with time (days) at 60 °C in a $H_2/O_2$ PEMFC. The empty and solid symbols refer, respectively, to the performance tested at the beginning and the end of each day. (b) Comparison of the performances of $Pd_{50}Pt_{30}Ni_{20}$ after becoming constant and after the durability test with that of commercial Pt at 60 °C in a $H_2/O_2$ PEMFC.

differences in the MEAs [11,40]. $Pd_{50}Pt_{30}Ni_{20}$ exhibits two times higher Pt-based mass activity than commercial Pt. However, since Pd is also a noble metal and much more expensive compared to Ni, it is more reasonable to compare the activity based on total noble metal mass. From Fig. 5(b) and Table 2, $Pd_{50}Pt_{30}Ni_{20}$ and commercial Pt have almost the same noble mass-based activity. Since the cost of Pd is less than half of that of Pt [65], the cost will be greatly reduced.

Considering the changes in performance with operating time, we were curious whether this novel catalyst will be durable enough for real fuel cell application. Accordingly, we ran the fuel cell for another two weeks with a total testing time of 200 h. Fig. 6 illustrates the cell voltage response with time at a constant load of 1000 mA $cm^{-2}$ during this period. The time shown in Fig. 6 does not include the time when the MEA is under open circuit potential or the polarization curve is recorded. Consistent with the performance change described above, the cell voltage for the $Pd_{50}Pt_{30}Ni_{20}$ catalyst shows significant increase within the first week. For a comparison, the cell voltage for pure Pt always remains constant at 0.680 V right after the activation procedure. After stabilizing at 0.676 V under 1000 mA $cm^{-2}$, the cell voltage of $Pd_{50}Pt_{30}Ni_{20}$ remains constant, and it decreases slightly from the 19th day (after 146 h in Fig. 6). The cell voltage tested on the 21st day is 0.655 V, indicating a loss of 3% and slightly worse durability compared to commercial Pt. We also compare the polarization-curve voltage of $Pd_{50}Pt_{30}Ni_{20}$ recorded on the last day with that in the initial constant curve in Fig. 4 (b). The kinetic activities of $Pd_{50}Pt_{30}Ni_{20}$ drawn in Tafel plots and listed in Table 2 show a decrease to ~35% of the initial value, which is much larger than that in the high cur-

**Table 2**
Mass activity of $Pd_{50}Pt_{30}Ni_{20}$ and commercial Pt catalysts.

| Catalyst | Annealing temp. (°C) | Mass activity at 0.84 V[a] ($A\,mg_{Pt}^{-1}$) | Mass activity at 0.84 V[a] ($A\,mg_{noble\ metal}^{-1}$) |
|---|---|---|---|
| $Pt_{100}$[b] | | 0.392 | 0.392 |
| $Pd_{50}Pt_{30}Ni_{20}$ | 300 | 0.739[c] | 0.369[c] |
| | | 0.269[d] | 0.134[d] |

[a] IR free data.
[b] 20 wt.% Pt on Vulcan Carbon.
[c] Initial constant performance.
[d] Performance after durability test.

rent density region, namely the ohmic-controlled region. It should be noticed that the degradation in performance, especially in the kinetic activity, is closely related to the decrease of the open circuit potential.

### 3.3. Effect of metal dissolution on MEA performance

To understand why the MEA performance increases continuously with operating time and eventually resembles that of commercial Pt, we tested both the surface and bulk composition of the $Pd_{50}Pt_{30}Ni_{20}$ catalyst before and after the fuel cell operation. Fig. 7 compares the XPS profiles of Pd 3d, Pt 4f, and Ni 2p recorded before the MEA operation (sample 1), after the MEA performance becomes constant (sample 2), and after the durability test (sample 3). As the typical mean free path for photoelectrons in alloys is in the range of 1–2 nm, XPS data are representative of several layers beneath the outermost surface. We should also point out that XPS tests were conducted using both an Al and Mg targets for samples after the fuel cell operation. The reason for the difference in operation is provided in the Supporting material (Fig. S1). The surface metal atomic ratios estimated from XPS profiles, together with the bulk metal atomic ratios determined from EDS, are summarized in Table 3 for all three samples.

In Fig. 7, Pd and Pt exist on the surface in both metal and oxide forms for all the three samples (the peaks are not deconvoluted here). As for Ni, all the peaks detected before the fuel cell test are attributed to Ni oxide (or hydroxide). It is clear from Fig. 7 and Table 3 that all the Ni on the catalyst surface is removed after the MEA test. At the same time, the bulk atomic percentage of Ni decreases from 12 before the test to 5 after the performance becomes constant, and finally to 0 after the durability test, indicating that even the Ni atoms below the surface leach out from the particles. Although the leaching becomes more difficult for the inner Ni and the rate of leaching slows down, Ni atoms eventually leach out of the particle totally. On the other hand, Pd on the surface also dissolves with time, as indicated by the deceasing Pd 3d peak intensity and the Pd:Pt ratio from >1 before the MEA test to <1 after the MEA test. Similar to Ni, Pd atoms may also leach out during the cell operation, but this point is more difficult to prove because the Ni dissolution and leaching will also change the Pd/Pt ratio in the bulk. However, it is clear that the rate of Pd dissolution decreases with time since the atomic percentage of Pd changes only by 10% after another 120 h of MEA test. Actually, Pt on the surface also dissolves to a small degree after the MEA testing for a longer time as indicated by the decreased intensity of the Pt 4f peak seen in Fig. 7(b).

If we take a further look at the compositions, we find that the catalyst before the MEA testing has a Ni-rich surface as indicated by a Ni atomic percentage of 21% on the surface and 12% in the whole

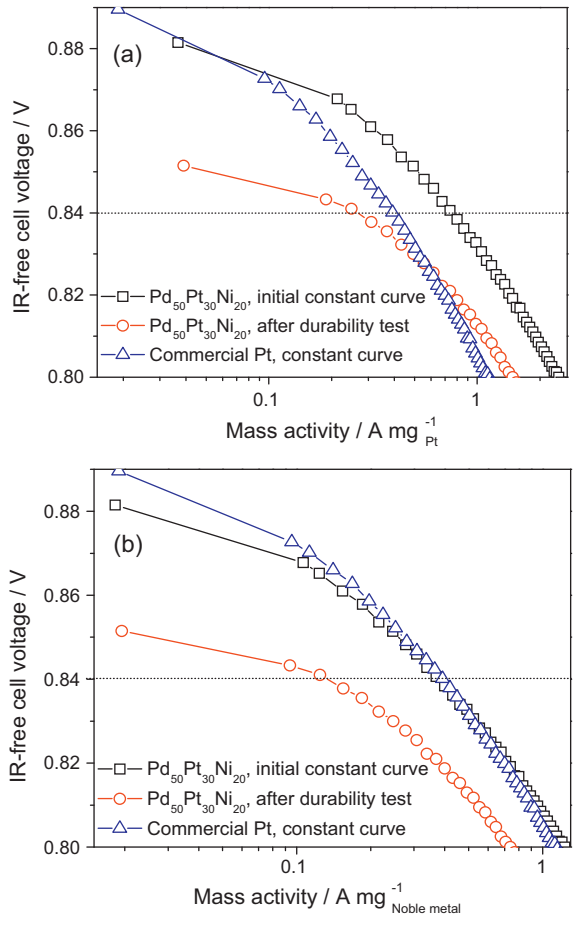


**Fig. 5.** Comparison of the Tafel plots of $Pd_{50}Pt_{30}Ni_{20}$ after the performance becomes constant and after the durability test with that of commercial Pt at 60 °C in a $H_2/O_2$ PEMFC: (a) cell voltage vs. Pt mass activity and (b) cell voltage vs. noble metal mass activity.

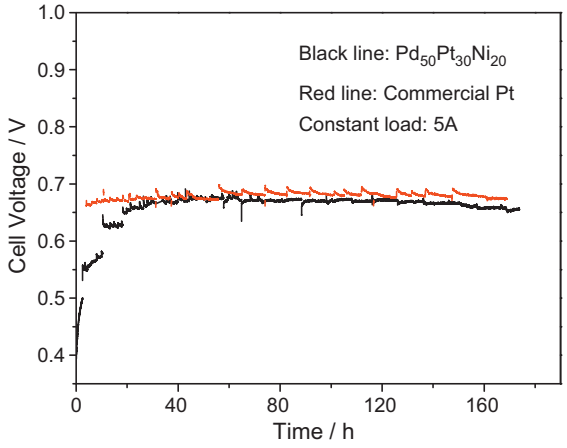


**Fig. 6.** The cell voltage response at the constant load of 1000 mA $cm^{-2}$ during the durability test. The solid line and the dashed lines refer, respectively, to $Pd_{50}Pt_{30}Ni_{20}$ and commercial Pt.

**Table 3**
Surface and bulk compositions of the 300 °C heat-treated $Pd_{50}Pt_{30}Ni_{20}$ catalysts.

| Catalyst | Testing condition | Near surface composition (XPS) (atom%) | Bulk composition (SEM-EDS) (atom%) |
|---|---|---|---|
| $Pd_{50}Pt_{30}Ni_{20}$ | Before the fuel cell test | $Pd_{49}Pt_{30}Ni_{21}$ | $Pd_{57}Pt_{31}Ni_{12}$ |
| | After performance becomes constant | $Pd_{46}Pt_{54}$ | $Pd_{54}Pt_{41}Ni_{5}$ |
| | After the durability test | $Pd_{41}Pt_{59}$ | $Pd_{58}Pt_{42}$ |

particle. On the contrary, the Pd/Pt ratio is below 1 on the surface and above 1 across the whole particle, indicating a structure with a Pt-rich surface and Pd-rich core for samples after the MEA testing. Therefore, we propose a structural model in Fig. 8 to account for the performance enhancement of the Pd–Pt–Ni electrocatalysts during the PEMFC single cell test.

The elemental distribution within the fresh catalyst is almost homogenous, and its surface is Pd-rich, resulting in lower activity and stability compared to that of pure Pt. On operating the MEA in the fuel cell, the electrocatalyst are subject to both chemical and electrochemical effects, and the metals have a tendency to dissolve. Particularly, base metals like Ni are not stable in contact with acid electrolyte. Under the single cell testing condition, the Ni atoms are also likely to segregate onto the particle surface due to the attraction to oxygen-containing species [66,67]. This could result in a continuous leaching out of Ni until all the Ni atoms within the particles are removed. For catalysts having a Ni-rich surface, like what we have here, this process is much easier and more rapid. In addition, the standard electroreduction potential of Pd (0.915 V) is much lower than that of Pt (1.188 V), resulting in an instability of Pd as well. In the oxygen and water environment in the fuel cell, the surface atoms can form an oxide or hydroxide overlayer, which can dissolve easily under the MEA testing conditions [68]. Moreover, the less-bonded Pd atoms can dissolve directly as Pd ions.

In our experiments, we test the single cell by shutting-down and starting-up cycles, in order to simulate a situation close to that of real fuel cell application. However, the 15 min of purging with nitrogen to remove the residual $H_2$ or $O_2$ after the load is removed in our experiments (see Section 2.3) will be different from the on/off procedures in real automotive applications. Nevertheless, during our shutting-down and starting-up cycles, the MEA will be subjected to more potential changes (also called load cycling), more start/stop cyclings, and more changes in temperature and humidity. Even Pt can dissolve more rapidly when undergoing such transitions from low to high potentials compared to a constant low or high potentials [69]. Moreover, starting and stopping the fuel cell, together with temperature and humidity changes, can considerably affect the rate of metal dissolution. This explains why the performance change between two sequential days is much larger than that within the same day. Considering a slow atom movement in the bulk compared to fast surface atom dissolution, we may expect a compositional gradient established across the particles. Eventually, an active dealloyed catalyst with a Pt-rich surface and a Pd-rich core structure is formed.

Within this core–shell structure, the lattice mismatch between the surface and core components will cause strain, which could modify the electronic properties of the surface, most notably their d band centers [29,70–72]. For a Pt-rich surface and Pd-rich core, the strain may downshift the d band center of the Pt-rich surface,

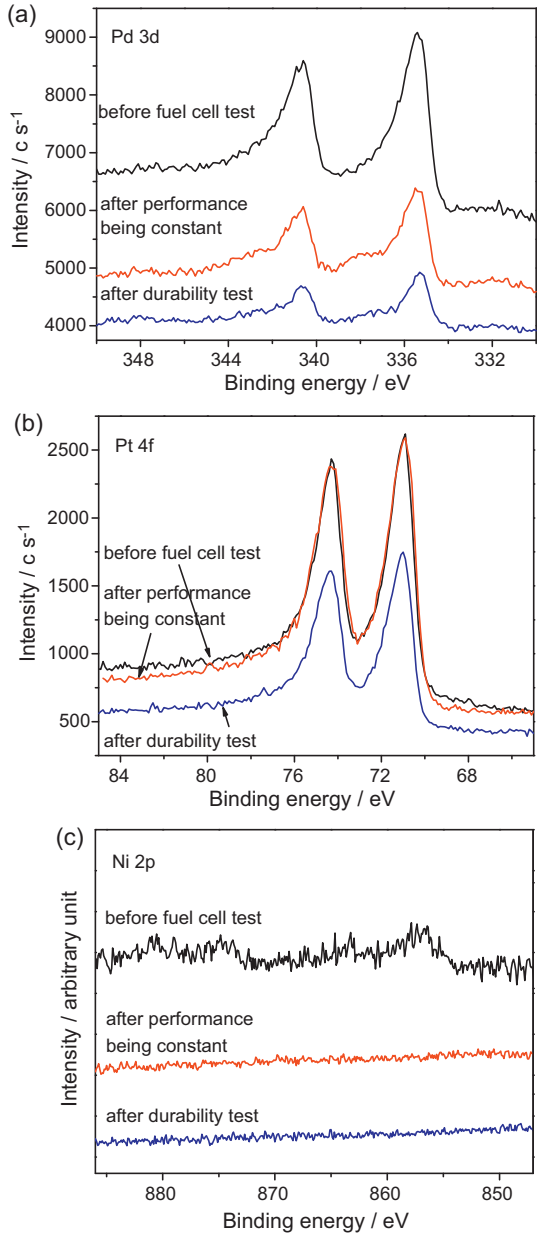


**Fig. 7.** Core level XPS profiles of (a) Pd 3d, (b) Pt 4f, and (c) Ni 2p in $Pd_{50}Pt_{30}Ni_{20}$ before the fuel cell test, after the performance becomes constant, and after the durability test.

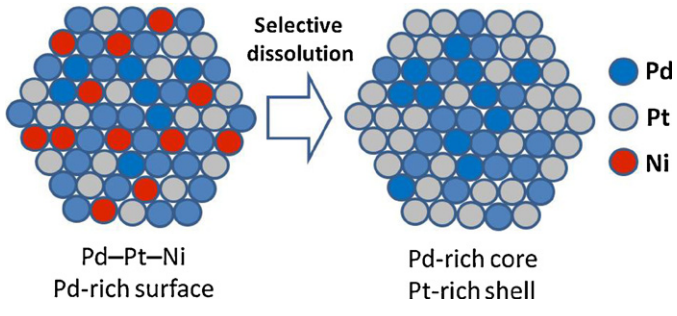


**Fig. 8.** Structure of Pd–Pt–Ni after the fuel cell test: formation of a Pd-rich core and Pt-rich shell nanoparticles by a dissolution of Pd and Ni (blue: Pd, grey: Pt, red: Ni). (For interpretation of the references to color in this figure legend, the reader is referred to the web version of the article.)

weaken the adsorption energy of the oxygenated intermediates, and thus enhance the ORR kinetics. The improved kinetic activity of the Pt-rich surface may also be attributed to a compression of the Pt–Pt bond distance [15,22,73–76]. It is worth pointing out that the Pt–M (M = transitional metal) electrocatalysts with a Pt skin may eventually lose all the M and the activity enhancement due to M and become eventually pure Pt-like [67]. In contrast, our Pd–Pt–Ni catalyst with Pd could still retain enhanced activity as Pd dissolution will be much less compared to the transition metals like Ni. We would also like to point out that the lattice parameter of the core is further decreased when Ni is present and the consequent larger mismatch between the core and shell components could lead to larger strain effect.

### 3.4. TEM analysis of the MEA before and after long-term durability test

As discussed before, although the $Pd_{50}Pt_{30}Ni_{20}$ electrocatalyst exhibits performance in the MEA test comparable to that of commercial Pt and the performance remains stable for more than 100 h, it eventually decreases slowly, especially in the activation polarization region, when the durability test prolongs to 200 h, suggesting lower stability compared to commercial Pt. We also discussed the dissolution and leaching out of both Pd and Ni metal ions from the catalyst nanoparticles. Naturally, one may ask where the metal ions go and the relationship between their dissolution and the MEA durability. Inductively coupled plasma (ICP) analysis data of the discharged water collected from the cathode side after the durability test indicated about 5 atom% of the total Ni in the water. Although Pd dissolution is found from the compositional changes, no Pd could be detected in the water.

To understand where the dissolved metal ions go, we analyzed the cross-section of the MEA by TEM before and after the durability test. Fig. 9(a) shows a TEM image of the middle part of the membrane after the fuel cell test. Many small particles and some agglomerations are found within the tested membrane, which were never seen in the fresh membrane. From the corresponding EDS data (Fig. 9(b)) of one particle circled in the TEM image, the particle was found to consist of Pd and Pt, mostly Pd, without any Ni. Thus, the dissolved Pd is redeposited in the membrane. Recognizing that cations can ion-exchange with the $H^+$ ions of the sulfonic acid groups in Nafion [11], we examined by EDS the area next to the circled region, and the result is shown in Fig. 9(c). The peak at 7.5 keV, which can only be ascribed to Ni, is clearly seen in this area of the membrane after the fuel cell test, and in fact, it is seen throughout the membrane afterwards. However, no signal for Ni could be seen in the fresh membrane. The data thus confirm that the dissolved base metal ions tend to attach to the hydrophilic sites at the sulfonic groups in the Nafion membrane by ion-exchange with proton. This type of ion exchange could also occur in the ionomer of the catalyst layer, but this was not explored.

Considering that only about 5 atom% Ni was detected by ICP in the discharged water, more Ni ions should be in the membrane. As pointed out by Gasteiger et al. [11], the ion exchange of protons by nickel ions could lead to the following: (i) lowering of the ionic conductivity of the membrane resulting in higher membrane resistance, (ii) increase in the resistance of the cathode catalyst layer due to higher ionomer resistance, and (iii) lower diffusion of oxygen in the ionomer in the catalyst layer. A combination of the above factors, which may be hard to separate, will essentially lower the overall performance and accelerate the degradation of the fuel cell. Refering back to our performance tests, the initial constant polarization curve of $Pd_{50}Pt_{30}Ni_{20}$ did not show any obvious decrease in the high current density region compared to Pt; in fact, it was a little bit better compared to Pt. Even after 200 h of operation, the polarization curve has slope similar to that of the initial curve, indicating

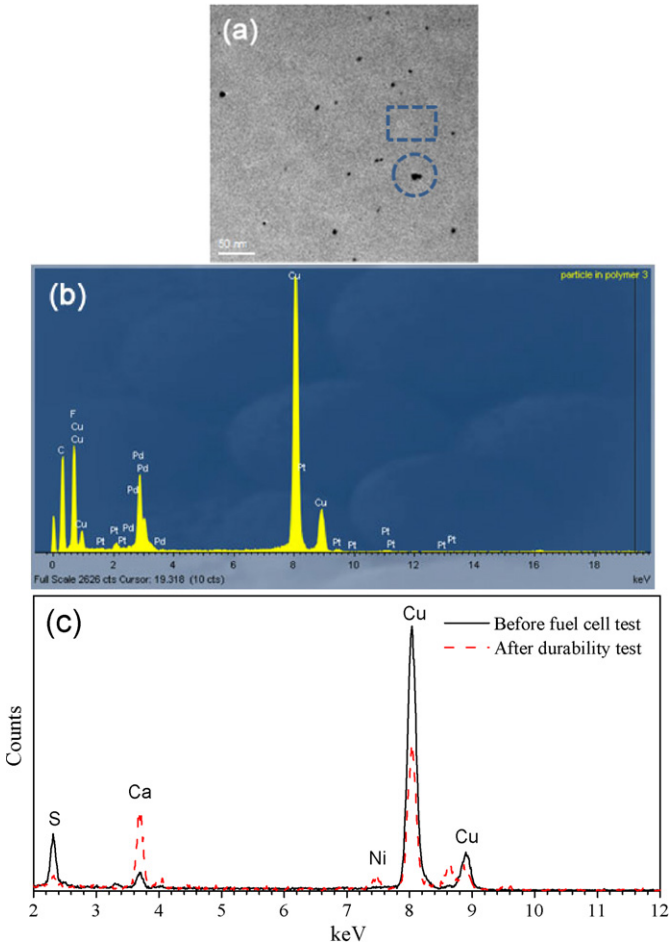


**Fig. 9.** (a) TEM image of the membrane from the MEA after the durability test at its center part, (b) EDS spectrum of the particle circled in the TEM image, and (c) EDS spectrum of the area within the rectangle in the TEM image. The peak in between the two Cu peaks and the peak marked as Ca are due to impurities.

a constant membrane resistance and a negligible effect of contaminaiton from Ni. However, the kinetic acitivity of cathode catalyst layer does decrease a lot, and this may be related to the poisoning by Ni cations.

To give a clear overview of the elemental distribution throughout the MEA, we ploted the compositions in each part of the MEA determined semi-quantitivly from the TEM-EDS tests of the MEA cross-sections before and after the durability test (Fig. 10). Compared to the fresh MEA, Ni is totally removed from the catalyst particles under the testing condition after the durability test, consistent with our previous results. Particles rich in palladium, with a small amount of platinum, are found not only at the center of the Nafion membrane, with a 2–3 μm strip, but also in the membrane along the membrane/cathode interface. Additionally, Pd has precipitated in the anode, but not as Pd rich particles. Bi et al. [77] have reported that soluble Pt ions formed at the cathode can be transported to the membrane by diffusion, migration, and possibly convection. They are re-deposited as Pt crystals upon reduction by hydrogen crossover, in a single thin Pt band instead of being uniform over a region between the edge of the band and the cathode. At that location, the hydrogen and oxygen are completely reacted, and the deposited Pt particles can be stable. We assume that a similar phenomenon happened here to the Pd ions, together with Pt ions. The difference is that a small amount of Pd and Pt ions are also deposited on the membrane/cathode interface. Besides, Pt ions in Bi et al.'s study could not move further toward the anode due

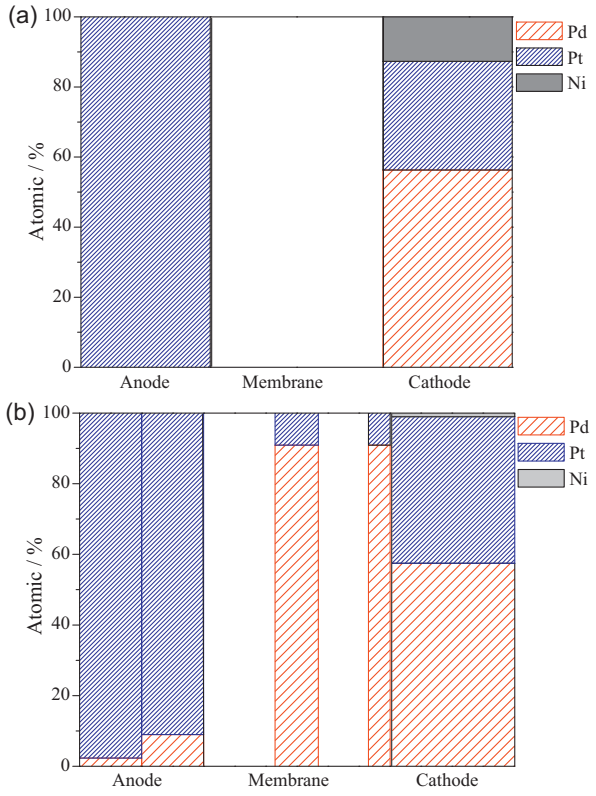


**Fig. 10.** Overall elemental distribution in the particles across the MEA: (a) before the fuel cell test and (b) after the durability test. Each bar represents the average atomic composition of particles in that area. The dark vertical lines indicate the interface between each electrode and the membrane. The anode in Fig. 10(b) has two elemental distributions to show the variation in composition as we approach the anode/membrane interface.

to pseudo-steady-state, but Pd ions here move continuously until they reach the anode. The Pd-rich particles in the membrane could result in lower proton conductivity, and the deposition of Pd on the anode would lead to a decrease in hydrogen oxidation activity. This may be one reason for the lower open circuit potential and thus the lower performance on the whole current region, especially kinetic region, after the durability test. Another possible reason for the lower open circuit potential may be the loss of the alloying effect due to the removal of all the Ni atoms from the catalyst after the durability test.

## 4. Conclusions

Pd–Pt–Ni electrocatalyst has been synthesized and the MEAs fabricated with Pd–Pt–Ni have been characterized before and after the PEMFC single cell test. XRD, EDS, and TEM analyses indicate the formation of Pd–Pt–Ni ternary alloy catalysts with a narrow size distribution centered at 5 nm. The PEMFC single cell test of the $Pd_{50}Pt_{30}Ni_{20}$ catalyst reveals a continuous increase in performance with operation time until it becomes comparable to that of commercial Pt. The catalyst is also quite stable within the 200 h of durability test, exhibiting just 3% degradation at 1000 mA $cm^{-2}$. With a lower cost and performance comparable to that of Pt, the Pd–Pt–Ni nanoalloy catalysts offer great promise.

Compositional analysis of the MEA before and after the fuel cell tests points to a Pd-rich core and a Pt-rich shell structure for the dealloyed particles formed under the fuel cell test condition. The strain effect caused by lattice mismatch between the Pd-rich core and the Pt-rich shell may down shift the d-band center, lower the adsorption energy of surface oxygenated intermediates, and thus enhance the surface catalytic activity. TEM observation of the MEA cross-section before and after fuel cell test also demonstrates an unfavorable effect of metal dissolution on MEA durability. Ni dissolves and leaches out of the catalyst particles completely. Except for a small amount of Ni in the water produced, most of the dissolved Ni ions ion-exchange with the protons in the Nafion membrane. In contrast, Pd dissolves partially, and the dissolved Pd ions re-precipitate as Pd-rich PdPt particles in the membrane, mainly forming a 2–3 μm band in the center and some along the cathode/membrane interface. Some Pd ions even move to the anode side and precipitate. All these factors could lead to contamination and degradation in the performance of MEAs.

The approach presented here is similar to the voltammetric dealloying used by Strasser's group [39,40] for modifying the surface catalytic properties of noble metal alloys. However, while the contamination by the base metals could be minimized by washing after dealloying, our future studies need to focus on alleviating or removing the poisoning effect caused by both Ni and Pd dissolution and their transport. Additionally, TEM data indicated a poor dispersion of Pd–Pt–Ni compared to Pt, and our future studies will focus on exploiting synthesis methods to obtain good dispersion as well on the effect of annealing temperature on the composition and performance.

## Acknowledgements

Financial support by the National Science Foundation grant CBET-0651929 and the Office of Naval Research MURI grant no. N00014-07-1-0758 is gratefully acknowledged.

## Appendix A. Supplementary data

Supplementary data associated with this article can be found, in the online version, at doi:10.1016/j.jpowsour.2011.01.026.

## References

[1] X. Li, Principles of Fuel Cells, Taylor-Francis, New York, 2006.
[2] R. O'hayre, S.-W. Cha, W. Colella, F.B. Prinz, Fuel Cell Fundamentals, Wiley, New York, 2006.
[3] B.C.H. Steele, A. Heinzel, Nature 414 (2001) 345.
[4] T.R. Ralph, M.P. Hogarth, Platinum Metals Rev. 46 (2002) 3.
[5] A.S. Aricò, S. Srinivasan, V. Antonucci, Fuel Cells 1 (2001) 133.
[6] S. Mukerjee, S. Srinivasan, J. Electroanal. Chem. 357 (1993) 201.
[7] V. Stamenkovic, B.S. Mun, M. Arenz, K.J.J. Mayerhofer, C.A. Lucas, G. Wang, P.N. Ross, N. Markovic, Nat. Mater. 6 (2007) 241.
[8] V. Stamenkovic, B.S. Moon, K.J. Mayerhofer, P.N. Ross, N. Markovic, J. Rossmeisl, J. Greeley, J.K. Norskov, Angew. Chem. Int. Ed. 45 (2006) 2897.
[9] V.R. Stamenkovic, B. Fowler, B.S. Mun, G. Wang, P.N. Ross, C.A. Lucas, N.M. Markovic, Science 315 (2007) 493.
[10] D. Thompsett, in: W. Vielstich, A. Lamm, H.A. Gasteiger (Eds.), Handbook of Fuel Cells—Fundamentals, Technology and Applications, Wiley, New York, 2003, p. 467.
[11] H.A. Gasteiger, S.S. Kocha, B. Sompalli, F.T. Wagner, Appl. Catal. B: Environ. 56 (2005) 9.
[12] R. Bashyam, P. Zelenay, Nature 443 (2006) 63.
[13] S. Mukerjee, S. Srinivasan, M.P. Soriaga, J. McBreen, J. Phys. Chem. 99 (1995) 4577.
[14] T. Toda, H. Igarashi, H. Uchida, M. Watanabe, J. Electrochem. Soc. 146 (1999) 3750.
[15] E. Antolini, R.R. Passos, E.A. Ticianelli, Electrochim. Acta 48 (2002) 263.
[16] U.A. Paulus, A. Wokaun, G.G. Scherer, T.J. Schmidt, V. Stamenkovic, N.M. Markovic, P.N. Ross Jr., Catal. Electrochim. Acta 47 (2002) 3787.
[17] U.A. Paulus, A. Wokaun, G.G. Scherer, T.J. Schmidt, V. Stamenkovic, V. Radmilovic, N.M. Markovic, P.N. Ross Jr., J. Phys. Chem. B 106 (2002) 4181.
[18] L. Xiong, A.M. Kannan, A. Manthiram, Electrochem. Commun. 4 (2002) 898.
[19] L. Xiong, A. Manthiram, J. Electrochem. Soc. 152 (2005) A697.
[20] J.R.C. Salgado, E. Antolini, E.R. Gonzalez, J. Phys. Chem. B 108 (2004) 17767.
[21] J.R.C. Salgado, E. Antolini, E.R. Gonzalez, J. Power Sources 141 (2005) 13.
[22] E. Antolini, J.R.C. Salgado, E.R. Gonzalez, J. Power Sources 155 (2006) 161.
[23] C.-J. Tseng, S.-T. Lo, S.-C. Lo, P.P. Chu, Mater. Chem. Phys. 100 (2006) 385.
[24] H. Yano, M. Kataoka, H. Yamashita, H. Uchida, M. Watanabe, Langmuir 23 (2007) 6438.
[25] E.I. Santiago, L.C. Varanda, H.M. Villullas, J. Phys. Chem. C 111 (2007) 3146.

[26] S. Koh, J. Leisch, M.F. Toney, P. Strasser, J. Phys. Chem. C 111 (2007) 3744.
[27] M.B. Vukmirovic, J. Zhang, K. Sasaki, A.U. Nilekar, F. Uribe, M. Mavrikakis, R.R. Adzic, Electrochim. Acta 52 (2007) 2257.
[28] R.R. Adzic, J. Zhang, K. Sasaki, M.B. Vukmirovic, M. Shao, J.X. Wang, A.U. Nilekar, M. Mavrikakis, J.A. Valerio, F. Uribe, Top. Catal. 46 (2007) 249.
[29] J. Zhang, M.B. Vukmirovic, Y. Xu, M. Mavrikakis, R.R. Adzic, Angew. Chem. Int. Ed. 44 (2005) 2132.
[30] J. Zhang, Y. Mo, M. Vukmirovic, R. Klie, K. Sasaki, R. Adzic, J. Phys. Chem. B 108 (2004) 10955.
[31] S.R. Brankovic, J.X. Wang, R.R. Adzic, Electrochem. Solid State Lett. 4 (2001) A217.
[32] I. Choi, O.J. Kwon, J.J. Kim, ECS Trans. 16 (2008) 1105.
[33] J. Yang, W. Zhou, C.H. Cheng, J.Y. Lee, Z. Liu, Appl. Mater. Interfaces 2 (2010) 119.
[34] A. Sarkar, A. Manthiram, J. Phys. Chem. C 114 (2010) 4725.
[35] M.H. Lee, J.S. Do, J. Power Sources 188 (2009) 353.
[36] W. Wang, R. Wang, S. Ji, H. Feng, H. Wang, Z. Lei, J. Power Sources 195 (2010) 3498.
[37] A. Sarkar, A.V. Murugan, A. Manthiram, Langmuir 26 (2010) 2894.
[38] S. Koh, P. Strasser, J. Am. Chem. Soc. 129 (2007) 12624.
[39] R. Srivastava, P. Mani, N. Hahn, P. Strasser, Angew. Chem. Int. Ed. 46 (2007) 8988.
[40] P. Mani, R. Srivastava, P. Strasser, J. Phys. Chem. C 112 (2008) 2770.
[41] K. Sasaki, J.X. Wang, H. Naohara, N. Marinkovic, K. More, H. Inada, R.R. Adzic, Electrochim. Acta 55 (2010) 2645.
[42] S. Ball, S.L. Burton, E. Christian, A. Davies, J. Fisher, R. O'Malley, S. Passot, B. Tessier, B.R.C. Theobald, D. Thompsett, ECS Trans. 25 (2009) 1011.
[43] D. Cao, A. Wieckowski, J. Inukai, N. Alonso-Vante, J. Electrochem. Soc. 153 (2006) A869.
[44] K.C. Lee, L. Zhang, J. Zhang, J. Electrochem. Commun. 9 (2007) 1704.
[45] K. Suárez-Alcántara, O. Solorza-Feria, J. Power Sources 192 (2009) 165.
[46] W. Xiao, D. Wang, X.W. Lou, J. Phys. Chem. C 114 (2010) 1694.
[47] J.H. Kim, A. Ishihara, S. Mitsushima, N. Kamiya, K.I. Ota, Electrochim. Acta 52 (2007) 2492.
[48] H. Liu, C. Song, Y. Tang, J. Zhang, Electrochim. Acta 52 (2007) 4532.
[49] R. Basyam, P. Zelenay, Nature 443 (2006) 63.
[50] A.L. Reddy, N. Rajalakshmi, S. Ramaprabhu, Carbon 46 (2008) 2.
[51] X.G. Yang, C.Y. Wang, Appl. Phys. Lett. 86 (2005) 224104.
[52] K. Lee, A. Ishihara, S. Mitsushima, N. Kamiya, K. Ota, Electrochim. Acta 49 (2004) 3479.
[53] H. Zhong, H. Zhang, Y. Liang, J. Zhang, M. Wang, X. Wang, J. Power Sources 164 (2007) 572.
[54] H. Zhong, H. Zhang, G. Liu, Y. Liang, J. Hu, B. Yi, Electrochem. Commun. 8 (2006) 707.
[55] J.L. Fernández, V. Raghuveer, A. Manthiram, A.J. Bard, J. Am. Chem. Soc. 127 (2005) 13100.
[56] A. Sarkar, A.V. Murugan, A. Manthiram, J. Phys. Chem. C 112 (2008) 12037.
[57] A. Sarkar, A.V. Murugan, A. Manthiram, J. Mater. Chem. 19 (2009) 159.
[58] L. Xiao, L. Zhuang, Y. Liu, J. Lu, H.D. Abruna, J. Am. Chem. Soc. 131 (2009) 602.
[59] J. Zhao, A. Sarkar, A. Manthiram, Electrochim. Acta 55 (2010) 1756.
[60] K. Juodkazis, J. Juodkazyt, B. Sebeka, G. Stalnionis, A. Lukinskas, Russ. J. Electrochem. 39 (2003) 954.
[61] M. Grdeń, M. Łukaszewski, G. Jerkiewicz, A. Czerwiński, Electrochim. Acta 53 (2008) 7583.
[62] V. Stamenkovic, T.J. Schmidt, P.N. Ross, N.M. Markovic, J. Phys. Chem. B 106 (2002) 11970.
[63] V. Stamenkovic, T.J. Schmidt, P.N. Ross, N.M. Markovic, J. Electroanal. Chem. 191 (2003) 554.
[64] P. Yu, M. Pemberton, P. Plasse, J. Power Sources 144 (2005) 11.
[65] http://www.platinum.matthey.com.
[66] C.A. Menning, H.H. Hwu, J.G. Chen, J. Phys. Chem. B 110 (2006) 15471.
[67] K. Hartl, K.J.J. Mayrhofer, M. Arenz, ECS Trans. 25 (2009) 555.
[68] E. Antolini, J.R.C. Salgado, E.R. Gonzalez, J. Power Sources 160 (2006) 957.
[69] R. Borup, J. Meyers, B. Pivovar, Y.S. Kim, R. Mukundan, N. Garland, D. Myers, M. Wilson, F. Garzon, D. Wood, P. Zelenay, K. More, K. Stroh, T. Zawodzinski, J. Boncella, J.E. McGrath, M. Inaba, K. Miyatake, M. Hori, K. Ota, Z. Ogumi, S. Miyata, A. Nishikata, Z. Siroma, Y. Uchimoto, K. Yasuda, K. Kimijima, N. Iwashita, Chem. Rev. 107 (2007) 3904.
[70] L.A. Kibler, A.M. El-Aziz, R. Hoyer, D.M. Kolb, Angew. Chem. Int. Ed. 44 (2005) 2080.
[71] V.R. Stamenkovic, B.S. Mun, K.J.J. Mayrhofer, P.N. Ross, N.M. Markovic, J. Am. Chem. Soc. 128 (2006) 8813.
[72] T. Bligaard, J.K. Norskov, Electrochim. Acta 52 (2007) 5512.
[73] M.-k. Min, J. Cho, K. Cho, H. Kim, Electrochim. Acta 45 (2000) 4211.
[74] E. Antolini, J.R.C. Salgado, M.J. Giz, E.R. Gonzalez, Int. J. Hydrogen Energy 30 (2005) 1213.
[75] M. Gattrell, B. MacDougall, in: W. Vielstich, H.A. Gasteiger, A. Lamm (Eds.), Handbook of Fuel Cells: Fundamentals, Technology and Applications, vol. 2, John Wiley & Sons Ltd., New York, 2003.
[76] S. Mukerjee, S. Srinivasan, M.P. Soriaga, J. Electrochem. Soc. 142 (1995) 1409.
[77] W. Bi, G.E. Gray, T.F. Fuller, Electrochem. Solid State Lett. 10 (2007) B101.